

MULTI-MODAL DOCUMENT PRESENTATION ATTACK DETECTION WITH FORENSICS TRACE DISENTANGLEMENT

Changsheng Chen¹, Yongyi Deng¹, Liangwei Lin¹, Zitong Yu^{2*}, Zhimao Lai³

¹Guangdong Key Laboratory of Intelligent Information Processing and Shenzhen Key Laboratory of Media Security, Shenzhen University, Shenzhen, China

²Great Bay University, Dongguan, China, ³China People’s Police University, Guangzhou, China

ABSTRACT

Document Presentation Attack Detection (DPAD) is an important measure in protecting the authenticity of a document image. However, recent DPAD methods demand additional resources, such as manual effort in collecting additional data or knowing the parameters of acquisition devices. This work proposes a DPAD method based on multi-modal disentangled traces (MMDT) without the above drawbacks. We first disentangle the recaptured traces by a self-supervised disentanglement and synthesis network to enhance the generalization capacity in document images with different contents and layouts. Then, unlike the existing DPAD approaches that rely only on data in the RGB domain, we propose to explicitly employ the disentangled recaptured traces as new modalities in the transformer backbone through adaptive multi-modal adapters to fuse RGB/trace features efficiently. Visualization of the disentangled traces confirms the effectiveness of the proposed method in different document contents. Extensive experiments on three benchmark datasets demonstrate the superiority of our MMDT method on representing forensic traces of recapturing distortion.

Index Terms— Document Image, Presentation Attack Detection, Multi-modality

1. INTRODUCTION

Document images record important information in human society. With the popularization of digital technology, many public sectors (such as finance and administration) serve society and citizens better through online services. To ensure the security of personal information and assets, online document (such as ID cards) authentication is required to confirm user identities in many cases. An Attacker may tamper the document image with photo editing tools and recapture (e.g., print and capture/scan) the tampered version to conceal the forgery traces. Therefore, Document Presentation Attack Detection (DPAD) is an important task to ensure the authenticity of document images.

Most existing works for recaptured image detection focus on face [1] and natural images [2], which are very different from DPAD tasks. For example, face anti-spoofing detection methods focus on the forensic traces in image depth and material, while no such traces can be found in the task of DPAD. In recent years, DPAD has attracted a lot of research focus and investigation. Chen *et al.* [3] proposed a three-input Siamese network to extract and compare the features of genuine and recaptured images. Li *et al.* [4] proposed a two-branch deep neural network that incorporates designed frequency filters and a multi-scale attention fusion module.

Some DPAD methods, such as [3], show limited generalization performance when evaluating document images with different contents and qualities. To mitigate this issue, [5, 6] proposed various distortion synthesis methods in spatial and spectral domains, respectively, to augment the recaptured features. The data synthesis method [5] introduces significant manual effort in collecting real recaptured traces. The F&B method [6] requires the knowledge of parameters in the recapturing devices (*i.e.*, resolutions of printing and imaging devices) during the training stage. Such prior knowledge is unavailable in many datasets, such as DLC2021 [7].

In this work, we propose the DPAD method with multi-modal disentangled traces (MMDT), which improves the generalization performance of existing DPAD methods *without requiring manual effort in collecting additional data or the knowledge of acquisition devices*.

First, inspired by the spoofing trace disentanglement techniques [8, 9] for face images, we propose to extract the recaptured traces from document images with an end-to-end disentanglement network. However, disentangling and transferring recaptured traces between document images with different contents and layouts is challenging. To improve the performance, we define the recaptured traces as blur content and texture components corresponding to the blurring and halftoning distortion, respectively, and design a self-supervised synthesis network that effectively transfers recaptured traces between various documents.

Second, contrary to [5, 6] that encourages recapturing feature extraction implicitly through data augmentation, we pro-

This work is sponsored by NSFC 62072313, 62371301, U23B2022, and the CCF-Alibaba Innovative Research Fund for Young Scholars. Z. Yu is the corresponding author.

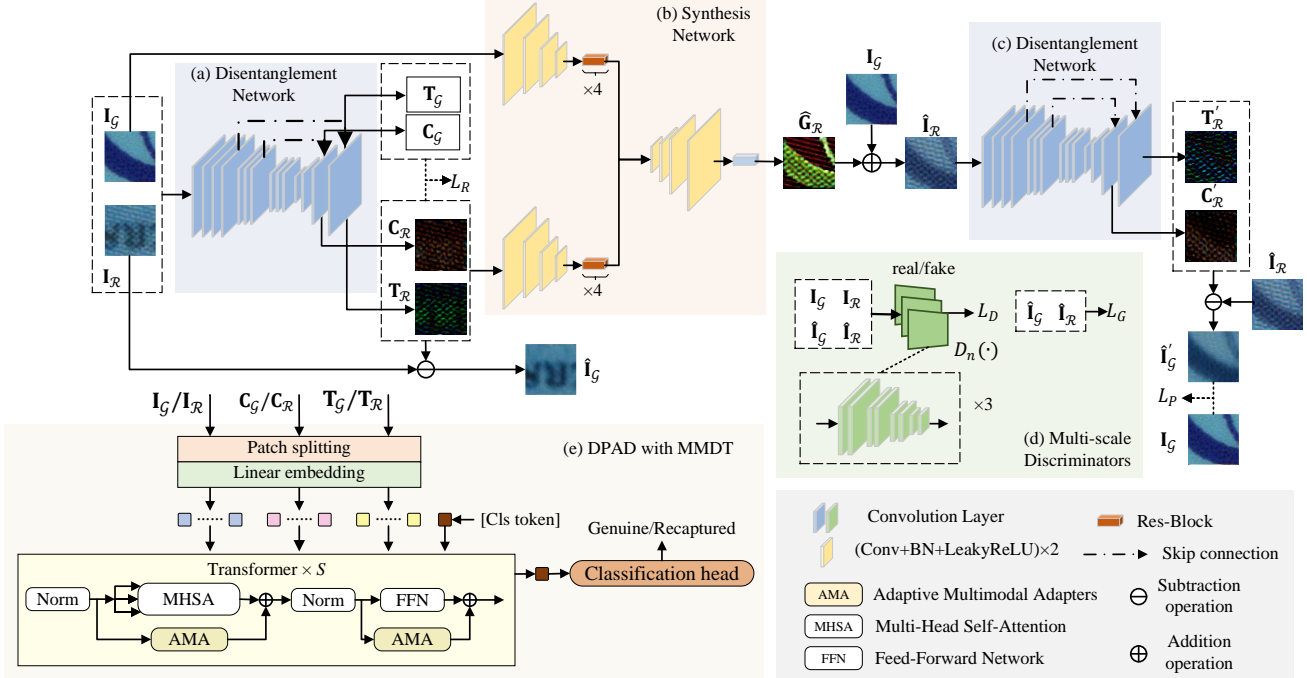


Fig. 1: The proposed DPAD network with disentangled recaptured traces. (a) Our disentanglement network disentangles the blur content \mathbf{C} and the texture \mathbf{T} from an image. (b) Our synthesis network synthesizes a recaptured trace $\hat{\mathbf{G}}_{\mathcal{R}}$ by spatially transforming the disentangled $\mathbf{C}_{\mathcal{R}}$ and $\mathbf{T}_{\mathcal{R}}$ in a recaptured image to fit the content of a genuine image $\mathbf{I}_{\mathcal{G}}$. (c) The disentanglement network (same as (a)) disentangles the blur content $\mathbf{C}'_{\mathcal{R}}$ and the texture $\mathbf{T}'_{\mathcal{R}}$ from $\hat{\mathbf{I}}_{\mathcal{G}}$. (d) The multi-scale discriminators classify real ($\mathbf{I}_{\mathcal{G}}; \mathbf{I}_{\mathcal{R}}$) or reconstructed ($\hat{\mathbf{I}}_{\mathcal{G}}; \hat{\mathbf{I}}_{\mathcal{R}}$) images. (e) The proposed DPAD method with multi-modal disentangled traces (MMDT), which takes $\mathbf{I}_{\mathcal{G}}$ or $\mathbf{I}_{\mathcal{R}}$ and its disentangled traces \mathbf{C}, \mathbf{T} as the input. During training, we finetuned the AMA and classification head while the parameters of the ViT backbone were frozen.

pose to explicitly employ the disentangled recaptured traces as new modalities in the DPAD task. The disentangled traces characterize the blurring and halftoning distortions, which are essential to the DPAD task. Thus, our multi-modal DPAD framework inputs the disentangled forensics traces and the RGB data to the transformer backbone and extracts distinctive features from different data modalities by adaptive multi-modal adapters (AMA) [10].

To demonstrate the cross-domain performance, we compare our method with a SOTA approach under document images covering various types and different collection devices. Visualization results confirm that the forensic traces disentangled by the proposed method are consistent with the recapturing distortion in the real document images. Quantitative results under a cross-domain protocol show that the proposed method outperforms the SOTA approach [6] (using RGB data only) by an improvement of average AUC and EER of 7.97% and 7.22 percentage points (p.p.), respectively.

The main contributions of this work are as follows.

- We propose a recaptured trace disentanglement network for document images with various contents by a self-supervised training strategy. Visualizations confirm that the proposed method achieves better performance on document images than an existing approach tailored for spoofing face images.
- We propose to explicitly fuse RGB features and recaptured traces in our DPAD network via lightweight multi-modal

adapters. It achieves better generalization performance than a SOTA approach on the latest DPAD image datasets, without requiring manual effort in collecting additional data or extra knowledge on the datasets.

- We extend the RSCID dataset [3] by incorporating 3,738 low-quality samples with blur and poor lighting, showing more practical application scenarios.

2. THE PROPOSED METHOD

This section introduces the framework of our forensics trace disentanglement and synthesis network, which is illustrated in Fig. 1. To show the contribution of this method, we focus on the trace disentanglement and recaptured image synthesis in Sec. 2.1 and 2.2.

2.1. Recaptured Trace Disentanglement Network

Inspired by the disentanglement of the spoof face [8, 9], recaptured traces for the DPAD task can be partitioned into multiple components based on their scale, *i.e.*, global traces, blur content traces, and texture traces. Global traces refer to color bias and color range disparities induced by recapture. Blur content traces represent the degradation of texture and characters in the original image caused by recapturing, including blurring distortions in the content, such as text, image, etc. Texture traces include the generation of fine textures such as halftone distortions from print-recapture. Different from

[8, 9], we do not consider global traces in our model since color distortion varies significantly across different document images. Thus, the disentangled recaptured traces $G(\mathbf{I})$ can be defined as

$$G(\mathbf{I}) = \lfloor \mathbf{C} \rfloor_N + \mathbf{T}, \quad (1)$$

where $\mathbf{C} \in \mathbb{R}^{L \times L \times 3}$ denotes the blur content traces, $\mathbf{T} \in \mathbb{R}^{N \times N \times 3}$ is the texture traces ($N > L$, N is the image size), and $\lfloor \cdot \rfloor$ is a resizing operation that upsizes \mathbf{C} to the same resolution of \mathbf{T} .

To supervise the disentanglement network, obtaining the ground truth of recaptured traces from a recaptured document image is not feasible. Therefore, we set a constraint on the disentangled results to facilitate the training of the disentanglement network. Specifically, we constraint that the magnitude of disentangled recaptured traces should be close to zero for a genuine image, while that should also be bounded for a recaptured image. This avoids any unnecessary changes to the document contents. Thus, the disentanglement process can be formulated as

$$G(\mathbf{I}) \approx \arg \min_{\hat{\mathbf{I}}} \|\mathbf{I} - \hat{\mathbf{I}}\|_F, \text{ s.t. } \mathbf{I} \in (\mathcal{G} \cup \mathcal{R}), \quad (2)$$

where the domain of genuine and recaptured images are denoted as $\mathcal{G} \subset \mathbb{R}^{N \times N \times 3}$ and $\mathcal{R} \subset \mathbb{R}^{N \times N \times 3}$, respectively, \mathbf{I} is the input image from either domain, $\hat{\mathbf{I}}_G$ is the reconstructed genuine image, and $\|\cdot\|_F$ takes the Frobenius norm.

Fig. 1 (a) illustrates the recaptured trace disentanglement network with an encoder-decoder architecture. The encoder applies a step-wise down-sampling process via convolution layers to the input image (genuine or recaptured), yielding an encoded feature in the latent space $\mathbf{F} \in \mathbb{R}^{28 \times 28 \times 96}$. The decoder up-samples the feature tensor \mathbf{F} with transposing convolution layers to generate the \mathbf{T} of the same size as the input image. Skip connections between the encoder and decoder preserve original image information, enhancing information flow and feature reconstruction. Feature tensors $\mathbf{C} \in \mathbb{R}^{56 \times 56 \times 3}$ are extracted at intermediate decoder layers.

2.2. Self-supervised Synthesis Network

After obtaining the disentangled recaptured traces extracted from recaptured images, we can apply them to genuine images, thus obtaining reconstructed recaptured samples. However, these recaptured traces contain content-related information associated with the source recaptured image. Applying the disentangled recaptured traces to genuine images with different content by the existing approaches [9] results in misalignment and strong visual artifacts, as visualized by results in Sec. 3.2.

To address such limitations, we propose a self-supervised synthesis network to perform spatial transformations on the recaptured traces. As shown in Fig. 1 (b), the inputs to the synthesis network include the recaptured features provided by $\mathbf{C}_{\mathcal{R}}$ and $\mathbf{T}_{\mathcal{R}}$, along with genuine images providing different content information. The synthesis network transfers

the $\mathbf{C}_{\mathcal{R}}$ and $\mathbf{T}_{\mathcal{R}}$ to fit the contents of \mathbf{I}_G and generate the re-constructed recaptured images. Specifically, the genuine image \mathbf{I}_G and recaptured traces $\mathbf{G}_{\mathcal{R}}$ are inputted into the encoder (consisting of convolution layers and batch normalization) respectively derive features $\mathbf{F}_G \in \mathbb{R}^{28 \times 28 \times 256}$ and $\mathbf{F}_{\mathcal{R}} \in \mathbb{R}^{28 \times 28 \times 256}$. The subsequent Res-Blocks capture and retain features from the inputs to enhance overall network performance. The decoder performs the inverse operation of the encoder. The decoded feature map undergoes a 3×3 convolutional layer to generate recaptured trace $\hat{\mathbf{G}}_{\mathcal{R}}$ that has spatially transformed according to the content in the genuine image \mathbf{I}_G .

To facilitate the training of our disentanglement and synthesis networks, we have made an important improvement in the pixel loss L_P , which self-supervises the disentanglement process. It is noted that the disentangled traces from real recaptured image $\mathbf{I}_{\mathcal{R}}$ and traces from reconstructed recaptured image $\hat{\mathbf{I}}_{\mathcal{R}}$ contain the same recaptured features but adapted to different image contents. The pixel loss in existing works [8, 9] cannot directly compare these recaptured traces. To address this limitation, we approach it from another perspective by computing the pixel loss of real genuine image \mathbf{I}_G and the pseudo-genuine image $\hat{\mathbf{I}}'_G$ (output from Fig. 1 (c)) in a self-supervise fashion. We define our pixel loss as

$$L_P = \mathbb{E}[\|\hat{\mathbf{I}}'_G - \mathbf{I}_G\|_1], \quad (3)$$

which verifies the effectiveness of the disentanglement network and enforces the reconstructed recaptured image $\hat{\mathbf{I}}_{\mathcal{R}}$ to have the same image content as the real genuine image \mathbf{I}_G .

To obtain reconstructed genuine and recaptured images, we design other loss functions following the settings in [8, 9]. Specifically, a regularization loss L_R is used to restrain the intensity of the disentangled traces, a discriminator loss L_D is used for distinguishing between the reconstructed images and the original images. Moreover, a generator loss L_G is used for ensuring that the recaptured image after recaptured trace disentanglement should be similar to a genuine image.

Finally, we define the total loss L of the disentanglement and synthesis network by including the regularizer loss L_R , the generator's loss L_G , the discriminative loss L_D , and the pixel loss L_P , which can be formulated as

$$L = \lambda_1 \cdot L_R + \lambda_2 \cdot L_G + \lambda_3 \cdot L_D + \lambda_4 \cdot L_P, \quad (4)$$

where $\lambda_1, \lambda_2, \lambda_3, \lambda_4$ are the weights to balance the loss from different components. More details on the loss functions are elaborated in the supplementary.

2.3. Multi-modal DPAD Network

After disentanglement of the recaptured traces, we propose to incorporate them explicitly in our DPAD model. Such direct inputs of recaptured traces to the network allow our model to focus on important information for the DPAD task. This is different from some SOTA approaches that encourage the implicit extraction of recaptured-related features through sample augmentation.

Inspired by the multi-modal methods in improving model performance and robustness [1, 10], we apply both the RGB images and the disentangled recaptured traces as multi-modal inputs to our DPAD network. Specifically, we utilize \mathbf{C} and \mathbf{T} obtained by the disentanglement network (Fig. 1 (a)) as two new modalities of the document image to perform multi-modal DPAD. This method is called DPAD with multi-modal disentangled trace, abbreviated as MMDT.

As illustrated in Fig. 1 (e), taking the ViT-B16 model as an example, we partition images of these three modalities into patches of 224×224 pixels to meet the network input size requirements. Then, the patches of each modality are flattened with a linear projection respectively. We connect the patch embeddings of each modality and feed the resulting sequence of vectors to the standard transformer encoder in the ViT-B16 model. To allow efficient information fusion across different data modalities, we adopt the adaptive multi-modal adapter (AMA) in our transformer backbone [10]. AMA is inserted into each transformer encoder as residual connections. In the whole network, we only finetune the AMA and the classification head while the parameters of other structures are fixed.

3. DATABASE AND EXPERIMENTAL RESULTS

3.1. Experimental Datasets

In the experiments, we use the following three datasets:

1) *Recaptured Student Card Image Dataset (RSCID)* [3]: The document images in this dataset are collected by 11 imaging devices and 3 printing devices. The templates for these samples are derived from student ID cards of 5 universities. Dataset \mathcal{D}_2 has 432 (48 genuine and 384 recaptured) samples collected by different imaging and printing devices. In the experiment, \mathcal{D}_2 in RSCID is employed as our training set.

2) *Recaptured Document Image Dataset with 162 templates (RDID162)* [6]: This dataset comprises 162 types of documents, including patent certificates, graduation certificates, transcripts, and licenses. It consists of 162 genuine images and 5,184 recaptured images. These image samples (all with resolutions higher than 1500×1500 pixels) are collected through 32 combinations of devices, consisting of 4 printing devices and 8 imaging devices (scanners and cameras). This dataset is employed as a testing set in our experiment.

3) *RSCID (L)*: We extended the original RSCID dataset with low-quality samples (denoted by ‘L’). Specifically, we collected 2,280 genuine and 1,458 recaptured images with low lighting, uneven illumination, bright spots, and laserjet printing distortions. This dataset is employed as a testing set in our experiment. More details of RSCID (L) are included in our supplementary material.

3.2. Recaptured Traces Disentanglement and Synthesis

In this part, we visualize the disentangled recaptured traces and the reconstructed recaptured image produced by our techniques in Sec. 2.1 and 2.2, respectively. This experiment uses the dataset \mathcal{D}_2 in RSCID. The dataset \mathcal{D}_2 is divided in an 8:1:1

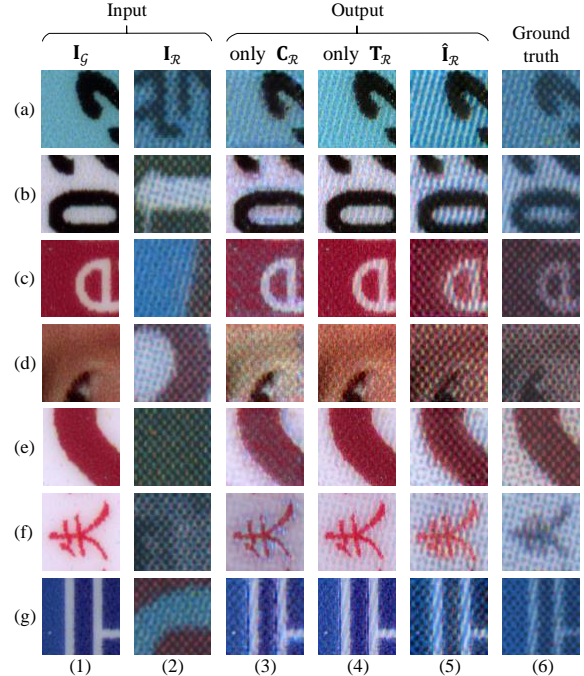


Fig. 2: Examples of reconstructed recaptured images. (1) Input genuine images \mathbf{I}_G that provide image content. (2) Input recaptured images \mathbf{I}_R that provide recaptured traces through disentanglement network. (3-5) Recaptured images reconstructed with component \mathbf{C}_R , \mathbf{T}_R and forensics traces $G(\mathbf{I})$, respectively. (6) Ground-truth recaptured images with the same contents as \mathbf{I}_G and acquired by the same devices as \mathbf{I}_R .

ratio for the training, validation, and testing sets, respectively. The proposed method is implemented on TensorFlow with an initial learning rate of 2×10^{-5} . Our model is trained in a total of 100K iterations with a batch size of 4. The parameters $\lambda_1, \lambda_2, \lambda_3, \lambda_4$ are set to be 1, 1, 1, 10, respectively. The details on the training process of our network are presented in Sec. 6 of the supplementary.

Columns (2) in Fig. 3 illustrates poor trace disentanglement results on recaptured images by [8]¹. In [8, 9], face shape and the position of facial features are marked with landmarks. These methods warp the spoofing traces into another facial templates by applying landmark offsets. However, transferring recaptured traces by warping is not feasible in document images since they have different contents and different landmarks. Following the same experimental setup, [8] can be applied to recaptured images but results in poor disentanglement performance. Due to the limitation of the 3D warping layer, the image disentanglement performance on recaptured images is less effective than that on spoof face images, making it less satisfactory.

As shown in columns (3) of Fig. 3, we successfully disentangle various recaptured traces. The disentangled trace $G(\mathbf{I})$ is the difference between the input image and its genuine re-

¹In our experiment, we consider the implementation provided by [8] since the source code of [9] is not available.

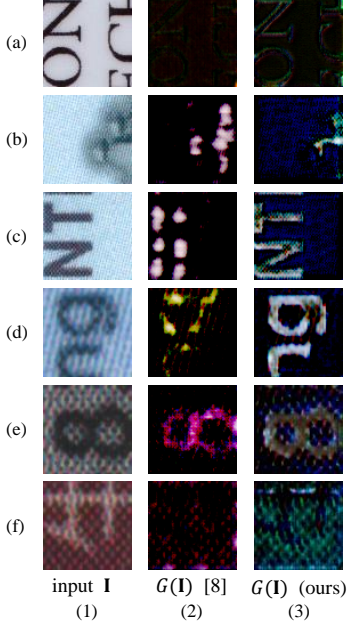


Fig. 3: Comparison of recaptured traces disentangled by [8] and our disentanglement network with self-supervision. (a) a genuine sample, (b-f) recaptured samples.

construction. As shown in Fig. 3 (b-g), halftone distortion (especially in the background region) is well detected in our $G(\mathbf{I})$. Although our method cannot restore image sharpness well when reconstructing genuine images, the model focuses on extracting effective forensic traces.

In Fig. 2, we show some examples of reconstructed recaptured images $\hat{\mathbf{I}}_{\mathcal{R}}$ using the disentangled recaptured traces. As shown in Fig. 2 (a-g), in our synthesis network, these recaptured traces can be transferred onto a genuine image $\mathbf{I}_{\mathcal{G}}$ without any semantic information of the recaptured document $\mathbf{I}_{\mathcal{R}}$. The reconstructed recaptured images $\hat{\mathbf{I}}_{\mathcal{R}}$ in column (5) generated by our synthesis network exhibit similar forged traces as those real recaptured images in column (6), which are recaptured using the same collection devices as those in column (2). This also reflects the effectiveness of the traces disentangled by our disentanglement network. Moreover, trace components $\mathbf{C}_{\mathcal{R}}$ and $\mathbf{T}_{\mathcal{R}}$ for $G(\mathbf{I})$ can be separately added to a genuine image, creating reconstructed genuine images with different styles. Compared to existing spoofing trace disentanglement methods for face images [8, 9], the proposed synthesis network effectively corrects the spatial geometric differences between the source recaptured traces and the target genuine image in the synthesis procedure.

3.3. Cross-Domain Experiment

In this part, we evaluate different DPAD approaches under three experimental protocols, *i.e.*, $\mathcal{D}_2 \rightarrow \text{RDID162}$, $\mathcal{D}_2 \rightarrow \text{RSCID (L)}$ and $\mathcal{D}_2 \rightarrow \text{ALL}$ (represents RDID162+RSCID

Table 1: Experiment results in cross-domain protocols. The symbol ‘ \rightarrow ’ indicates the training set (\mathcal{D}_2) on the left and the test set on the right. ALL represents RDID162+RSCID (L). The best performance (with EER as the primary evaluation metric) first and second in each modality are respectively **bold-faced** and underlined.

Protocols Methods	$\mathcal{D}_2 \rightarrow \text{RDID162}$		$\mathcal{D}_2 \rightarrow \text{RSCID (L)}$		$\mathcal{D}_2 \rightarrow \text{ALL}$	
	AUC	EER	AUC	EER	AUC	EER
Modality: RGB						
CDCN [11]	0.6806	38.78%	0.4361	54.51%	0.6803	35.96%
ViT [12]	0.8433	23.12%	0.8590	23.16%	0.8121	26.24%
BeiT-B [13]	0.8517	22.80%	0.9339	14.88%	<u>0.8349</u>	<u>24.14%</u>
ViT+F&B [6]	0.8457	21.65%	0.8900	18.30%	0.8450	20.92%
BeiT-B+F&B [6]	0.8043	28.27%	0.8873	20.49%	0.6446	40.32%
Modality: RGB+C						
MM-CDCN [14]	0.7290	35.19%	0.4921	43.10%	0.7702	29.39%
ViT [12]	0.8789	20.36%	0.8635	21.83%	0.8382	25.01%
BeiT-B [13]	0.7604	32.02%	0.8298	24.95%	0.8202	26.33%
ViT+MMDT	0.8901	19.04%	<u>0.8777</u>	<u>20.24%</u>	<u>0.8805</u>	<u>20.51%</u>
BeiT-B+MMDT	<u>0.8861</u>	<u>19.28%</u>	0.9405	13.16%	0.8940	19.04%
Modality: RGB+T						
MM-CDCN [14]	0.6320	40.16%	0.6240	42.44%	0.8346	24.87%
ViT [12]	0.8725	21.71%	0.8850	18.99%	0.8385	24.23%
BeiT-B [13]	0.8127	27.27%	0.8638	21.70%	0.8533	22.88%
ViT+MMDT	0.9149	15.57%	0.9106	16.30%	0.8628	20.84%
BeiT-B+MMDT	<u>0.8816</u>	<u>19.83%</u>	0.9350	14.98%	0.9036	17.53%
Modality: RGB+C+T						
MM-CDCN [14]	0.7089	34.53%	0.6177	43.46%	0.8147	27.58%
ViT [12]	0.8849	19.65%	0.8999	18.61%	0.8298	23.66%
BeiT-B [13]	0.7311	33.90%	0.8356	25.08%	0.8188	26.12%
ViT+MMDT	0.9180	16.02%	<u>0.9231</u>	<u>16.56%</u>	<u>0.8683</u>	<u>20.44%</u>
BeiT-B+MMDT	0.8740	19.14%	0.9452	12.53%	0.8847	18.75%

(L)). The training and testing sets cover different acquisition devices and diverse document types. $\mathcal{D}_2 \rightarrow \text{RDID162}$ shows a practical application scenario in which our model is trained on a small and constrained dataset while the testing images in 162 templates are gathered under diverse conditions. The $\mathcal{D}_2 \rightarrow \text{RSCID (L)}$ protocol demonstrates the performance under low-quality scenarios. Dataset \mathcal{D}_2 of RSCID is split in an 8:2 ratio to form the training and validation sets, and the RDID162 and RSCID (L) datasets are employed for testing.

We compare the performances of different approaches with the proposed MMDT in this experiment. For the single-modal case, we consider one CNN model (CDCN [11]) and two transformer backbones (ViT-B16 model [12] and BeiT-B model [13]). For multi-modal cases (RGB+C, RGB+T, RGB+C+T), we use the multi-modal implementations of these models, *i.e.*, multi-modal CDCN [14], multi-modal ViT-B16 [10] and multi-modal BeiT-B (both with and without MMDT). It is noted that [8] is not considered in this experiment due to the poor performance of recaptured trace disentanglement shown in Sec. 3.2.

These networks utilize input image patches of size 224×224 pixels and are trained using the Adam optimizer with a batch size of 64. ImageNet pre-trained weights are used for our transformer encoder. For AMA fine-tuning, the number of original and hidden channels are 768 and 64, respectively. Fine-tuning of the model lasts up to 30 epochs with a learning rate of 1×10^{-4} , a weight decay of 0.05, and cross-entropy

loss. All methods achieve an image-level decision by a majority voting of the patch-level ones. Performance is evaluated using the Area Under the ROC Curve (AUC) and Equal Error Rate (EER) metrics.

As shown in Tab. 1, for the single-modality approach (RGB-only), the performances across the protocols are not stable. After performing data augmentation by a SOTA DPAD approach, F&B [6], the performance for most backbones yields better results than those without F&B. However, under the $\mathcal{D}_2 \rightarrow \text{ALL}$ protocol, the AUC and EER of the BeiT-B+F&B model dropped by 0.1903 and 16.18 percentage points (p.p.) compared to those of the BeiT-B model. The unstable performance of the BeiT-B model is due to the limitation of the pre-training task in this model [15].

In the case of multi-modal scenarios (RGB+C, RGB+T, and RGB+C+T), especially for the protocol $\mathcal{D}_2 \rightarrow \text{ALL}$, MM-CDCN shows an average performance improvement of 0.1262 and 8.68 p.p. compared to those in RGB-only mode. This emphasizes that the traces disentangled by our method contribute to enhancing the model’s performance in complex scenarios.

For the bimodal scenarios (RGB+C and RGB+T), the performance of the methods is generally improved compared to those in RGB-only mode. In the settings with RGB+T modality, the average AUC and EER of the methods have increased by 0.0185 and 2.01 p.p., 0.0424 and 3.39 p.p., 0.0933 and 7.42 p.p., respectively, compared to those in RGB-only mode for each protocol ($\mathcal{D}_2 \rightarrow \text{RDID162}$, $\mathcal{D}_2 \rightarrow \text{RSCID (L)}$, $\mathcal{D}_2 \rightarrow \text{ALL}$). Especially for the backbones with MMDT, there is a noticeable performance improvement compared to the SOTA method (*i.e.*, F&B [6]).

For the tri-modal scenarios, our methods achieve better performance than those in dual-modality mode under $\mathcal{D}_2 \rightarrow \text{RSCID (L)}$ protocol, while our methods with dual-modal and tri-modal configurations perform comparably under the protocols of $\mathcal{D}_2 \rightarrow \text{RDID162}$ and $\mathcal{D}_2 \rightarrow \text{ALL}$. This suggests that, by integrating the recaptured traces **C** and **T**, the trained models are more robust under low-quality scenarios.

4. CONCLUSION

This work proposes a DPAD network, MMDT, via information disentanglement and multi-modal learning techniques. The experimental results confirm that our MMDT method provides better disentanglement results and achieves better generalization performance under challenging protocols.

In the future, we plan to extend our research toward the disentanglement of different forensic traces, such as forgery. The forgery traces include artifacts in edge, font, and background textures. The successful disentanglement of such traces will be helpful in a wide range of document image forensic tasks.

5. REFERENCES

- [1] Ajian Liu, Zichang Tan, Jun Wan, Yanyan Liang, Zhen Lei, Guodong Guo, and Stan Z Li, “Face anti-spoofing via adversarial cross-modality translation,” *IEEE TIFS*, vol. 16, pp. 2759–2772, 2021.
- [2] Haoliang Li, Shiqi Wang, and Alex C Kot, “Image recapture detection with convolutional and recurrent neural networks,” *EI*, vol. 2017, no. 7, pp. 87–91, 2017.
- [3] Changsheng Chen, Shuzheng Zhang, Fengbo Lan, and Jiwu Huang, “Domain-agnostic document authentication against practical recapturing attacks,” *IEEE TIFS*, vol. 17, pp. 2890–2905, 2022.
- [4] Jiaying Li, Chenqi Kong, Shiqi Wang, and Haoliang Li, “Two-branch multi-scale deep neural network for generalized document recapture attack detection,” in *ICASSP*, 2023, pp. 1–5.
- [5] Daniel Benalcazar, Juan E Tapia, Sebastian Gonzalez, and Christoph Busch, “Synthetic id card image generation for improving presentation attack detection,” *IEEE TIFS*, vol. 18, pp. 1814–1824, 2023.
- [6] Changsheng Chen, Bokang Li, Rizhao Cai, Jishen Zeng, and Jiwu Huang, “Distortion model-based spectral augmentation for generalized recaptured document detection,” *IEEE TIFS*, vol. 19, pp. 1283–1298, 2023.
- [7] Dmitry V Polevoy, Irina V Sigareva, Daria M Ershova, Vladimir V Arlazarov, Dmitry P Nikolaev, Zuheng Ming, Muhammad Muzzamil Luqman, and Jean-Christophe Burie, “Document liveness challenge dataset (DLC-2021),” *Journal of Imaging*, vol. 8, no. 7, pp. 181, 2022.
- [8] Yaojie Liu, Joel Stehouwer, and Xiaoming Liu, “On disentangling spoof trace for generic face anti-spoofing,” in *ECCV*. Springer, 2020, pp. 406–422.
- [9] Yaojie Liu and Xiaoming Liu, “Spoof trace disentanglement for generic face anti-spoofing,” *IEEE TPAMI*, vol. 45, no. 3, pp. 3813–3830, 2022.
- [10] Zitong Yu, Rizhao Cai, Yawen Cui, Xin Liu, Yongjian Hu, and Alex Kot, “Rethinking vision transformer and masked autoencoder in multimodal face anti-spoofing,” *IJCV*, 2024.
- [11] Zitong Yu, Chenxu Zhao, Zezheng Wang, Yunxiao Qin, Zhuo Su, Xiaobai Li, Feng Zhou, and Guoying Zhao, “Searching central difference convolutional networks for face anti-spoofing,” in *CVPR*, 2020, pp. 5295–5305.
- [12] Alexey Dosovitskiy, Lucas Beyer, Alexander Kolesnikov, Dirk Weissenborn, Xiaohua Zhai, Thomas Unterthiner, Mostafa Dehghani, Matthias Minderer, Georg Heigold, Sylvain Gelly, Jakob Uszkoreit, and Neil Houlsby, “An image is worth 16×16 words: Transformers for image recognition at scale,” in *ICLR*, 2021.
- [13] Hangbo Bao, Li Dong, Songhao Piao, and Furu Wei, “Beit: Bert pre-training of image transformers,” in *ICLR*, 2022.
- [14] Zitong Yu, Yunxiao Qin, Xiaobai Li, Zezheng Wang, Chenxu Zhao, Zhen Lei, and Guoying Zhao, “Multi-modal face anti-spoofing based on central difference networks,” in *CVPRW*, 2020, pp. 650–651.
- [15] Yunjie Tian, Lingxi Xie, Zhaozhi Wang, Longhui Wei, Xiaopeng Zhang, Jianbin Jiao, Yaowei Wang, Qi Tian, and Qixiang Ye, “Integrally pre-trained transformer pyramid networks,” in *CVPR*, 2023, pp. 18610–18620.

6. SUPPLEMENTARY MATERIAL

6.1. The Synthesis Network Details

As shown in Tab. S1 - S3, we introduce the structure of different components in our synthesis network.

Table S1: Convolution-BatchNorm-LeakyReLU Block (Conv + BN + LeakyReLU)

Layer name	Layer content
Conv	Conv (3×3 , 32 channels, no activation)
BN	Batch Normalization: Normalize the output
Activation	LeakyReLU Activation

Table S2: Encoder Block

Layer name	Layer content
Conv1-1	Conv-BN-LeakyReLU Block (32 channels)
Conv1-2	Conv-BN-LeakyReLU Block (32 channels)
Pool1	Conv (3×3 , strides=2, activation=LeakyReLU): Increase channels to 64
Conv2-1	Conv-BN-LeakyReLU Block (64 channels)
Conv2-2	Conv-BN-LeakyReLU Block (64 channels)
Pool2	Conv (3×3 , strides=2, activation=LeakyReLU): Increase channels to 128
Conv3-1	Conv-BN-LeakyReLU Block (128 channels)
Conv3-2	Conv-BN-LeakyReLU Block (128 channels)
Pool3	Conv (3×3 , strides=2, activation=LeakyReLU): Increase channels to 256
Conv4-1	Conv-BN-LeakyReLU Block (256 channels)
Conv4-2	Conv-BN-LeakyReLU Block (256 channels)

Table S3: Decoder Block

Layer name	Layer content
Conv1-1	Conv-BN-LeakyReLU Block (256 channels)
Conv1-2	Conv-BN-LeakyReLU Block (256 channels)
Deconv1	Transpose Conv (3×3 , strides=2, activation=LeakyReLU)
Conv2-1	Conv-BN-LeakyReLU Block (128 channels)
Conv2-2	Conv-BN-LeakyReLU Block (128 channels)
Deconv2	Transpose Conv (3×3 , strides=2, activation=LeakyReLU)
Conv3-1	Conv-BN-LeakyReLU Block (64 channels)
Conv3-2	Conv-BN-LeakyReLU Block (64 channels)
Deconv3	Transpose Conv (3×3 , strides=2, activation=LeakyReLU)
Conv4-1	Conv-BN-LeakyReLU Block (32 channels)
Conv4-2	Conv-BN-LeakyReLU Block (32 channels)

6.2. Discriminators and Loss Function

6.2.1. Multi-scale Discriminators

As shown in Fig. 1 (d), we apply discriminative supervision on the reconstructed images to ensure the visual quality of reconstructed images. Discriminative supervision is used for distinguishing between the reconstructed images ($\hat{\mathbf{I}}_G; \hat{\mathbf{I}}_R$) and the real images ($\mathbf{I}_G; \mathbf{I}_R$). Simultaneously, under discriminative supervision, the disentanglement network aims to produce realistic images, while the recaptured images after re-

captured trace disentanglement are classified as real images. To overcome the limited receptive field of a single discriminator for large-scale images, we utilize multi-scale discriminators $D_n(\cdot)$, $n = \{1, 2, 3\}$ at different resolutions (224×224 , 112×112 , and 56×56 pixels) to allow the focus on different texture scales. Each discriminator consists of 8 convolutional layers, including 3 downsampling operations.

6.2.2. The Loss Functions

We introduce the loss functions that are not explicitly provided in the main text.

According to Eq. (2), we need to minimize the intensity of forensics traces. these traces satisfy certain domain conditions. This regularizer loss L_R is written as

$$L_R = \alpha_1 \cdot \mathbb{E} \left[\|G(\mathbf{I}_G)\|_2^2 \right] + \alpha_2 \cdot \mathbb{E} \left[\|G(\mathbf{I}_R)\|_2^2 \right], \quad (5)$$

where parameters α_1 and α_2 are set to be 10 and 1×10^{-4} , respectively.

Discriminators should distinguish the real images and the reconstructed images. For the discriminator supervision, the discriminative loss can be formulated as

$$L_D = \sum_{n=1,2,3} \left\{ \mathbb{E} \left[(D_n(\mathbf{I}_G) - 1)^2 \right] + \mathbb{E} \left[(D_n(\hat{\mathbf{I}}_G))^2 \right] + \mathbb{E} \left[(D_n(\mathbf{I}_R) - 1)^2 \right] + \mathbb{E} \left[(D_n(\hat{\mathbf{I}}_R))^2 \right] \right\}, \quad (6)$$

where the first two terms in the equation represent distinguishing between the real and reconstructed genuine samples, while the last two terms represent distinguishing between the real and reconstructed recaptured samples.

The generator's loss function can be expressed as

$$L_G = \sum_{n=1,2,3} \left\{ \mathbb{E} \left[(D_n(\hat{\mathbf{I}}_G) - 1)^2 \right] + \mathbb{E} \left[(D_n(\hat{\mathbf{I}}_R) - 1)^2 \right] \right\}, \quad (7)$$

where the reconstructed images $\hat{\mathbf{I}}_G, \hat{\mathbf{I}}_R$ are treated as real images and are discriminated against by the multi-scale discriminators.

6.3. Training of Disentanglement and Synthesis Network

The training process of disentanglement and synthesis network can be divided into 3 parts.

1) **Generation part.** Input images (\mathbf{I}_G and \mathbf{I}_R) are fed into the disentanglement and synthesis network with loss functions L_G and L_R , resulting in reconstructed images $\hat{\mathbf{I}}_G$ and $\hat{\mathbf{I}}_R$.

2) **Self-supervision part.** In this part, the pixel loss L_P is computed between the pseudo-genuine image $\hat{\mathbf{I}}'_G$ and the real genuine image \mathbf{I}_G , establishing a self-supervised process.



Fig. S1: Examples of document images in RSCID by [3] and our RSCID (L).

Table S4: The devices used for collecting RSCID (L).

1st Imaging Devices	Printer Devices	2nd Imaging Devices
HUAWEI HONOR 10 (24 MP)	Canon C3530 600 DPI	Honor 50SE (12 MP)
HUAWEI HONOR 30 (40MP)		Iqoo Z5 (12 MP)
HUAWEI P30 (40 MP)		OPPO K9x (12 MP)
iPhone 14 Pro Max (48 MP)		

3) **Discriminator part.** The multi-scale discriminators are trained to classify the real ($\mathbf{I}_G; \mathbf{I}_R$) or reconstructed ($\hat{\mathbf{I}}_G; \hat{\mathbf{I}}_R$) images with the discriminator loss L_D .

During the training process, execute parts 1) 2) 3) every even-numbered epoch and parts 1) 2) every odd-numbered epoch until training stops. It should be noted that, within each epoch, the disentanglement network in Fig. 1 (a) undergoes parameter updates, while it is frozen in Fig. 1 (c) after being updated in Fig. 1 (a).

6.4. Our RSCID (L) Dataset

Given that datasets \mathcal{D}_1 and \mathcal{D}_2 in RSCID were collected only under normal lighting conditions, we find it necessary to collect a new dataset, denoted as RSCID (L), to do the robust

evaluation of DPAD approaches under various distortion scenarios.

Tab. S4 reports all the devices used in our extended low-quality samples. The process of collecting recaptured document images follows the rules outlined in [3], except that we consider some poor lighting conditions. We shoot the documents under different lighting conditions (direct light, dark weak light, and normal light sources), introducing various noise distortions in the captured document images. Direct light conditions involve exposing the original documents to direct light sources, resulting in captured document images with noticeable glares and shadows. Dark weak light conditions aim to capture original documents in a dark environment, preserving only dim light sources that do not directly illuminate the original document. Document images captured under normal light source conditions typically do not exhibit noticeable glare, and the image information is clear and sharp.

Some examples of document images are shown in Fig. S1. The low-quality samples consist of student ID cards with 18 different content templates. There are six additional templates compared to datasets \mathcal{D}_1 and \mathcal{D}_2 , all of which are real student ID cards. We manually crop documents from a white background. The resolutions of the cropped genuine document images range from 1260×793 pixels to 3382×2151 pixels, while those of the cropped recaptured document images range from 820×690 pixels to 3911×1658 pixels.